Upstream Internal Hydraulic Jumps

PATRICK F. CUMMINS

Institute of Ocean Sciences, Sidney, British Columbia, Canada

LAURENCE ARMI

Scripps Institution of Oceanography, La Jolla, California

SVEIN VAGLE

Institute of Ocean Sciences, Sidney, British Columbia, Canada

(Manuscript received 1 February 2005, in final form 29 September 2005)

ABSTRACT

In stratified tidal flow over a sill, the character of the upstream response is determined by a Froude number F_s based on the stratification near the surface. This is distinguished from the Froude number governing the response in the neighborhood of the sill crest, which is based on the weak density step associated with a flow bifurcation. For moderate values of F_s, the upstream response consists of nonlinear waves or a weak undular bore. For larger values of F_s, a strong, quasi-stationary, internal hydraulic jump dominates the upstream response. At sufficiently large values of F_s, the upstream bore is swept downstream and lost. Acoustic backscatter and velocity data are presented for the case of a strong internal bore or gravity current in a tidally modulated sill flow. Numerical simulations with varying near-surface stratification are presented to illustrate the upstream responses at different values of F_s. The theory of two-layer hydraulic flows is invoked to account for the development of the upstream jump.

1. Introduction

Stratified flows over large-amplitude topography are known to be associated with the generation of finite-amplitude internal waves and bores. While such disturbances have now been observed frequently and in many distinct locations, the details of the generation in natural settings are not well understood. The observed wave trains, for example in photographs and satellite imagery (Jackson 2004), are often located in the far field, leading to uncertainty in identifying generation sites and mechanisms.

Steepening of shoreward-propagating internal tides has been identified as one possible mechanism for the occurrence of internal bores and nonlinear waves over continental shelves (e.g., Holloway et al. 1997). The laboratory experiments of Maxworthy (1979) provide a model for the generation of nonlinear or solitary waves that is applicable to tidal flows over sills or submarine ridges. These experiments show the formation of a large pycnocline depression on the downstream side of the sill. As the tide slackens, the pycnocline depression advances and disintegrates into a group of rank-ordered solitons over the sill. While the advance of the massive pycnocline depression has been observed in field studies, nonlinear wave trains are also observed to form much earlier and apparently independently of the collapse of the downstream structure (e.g., Farmer and Armi 1999b; Cummins et al. 2003).

In this paper we present new observations taken over a sill that illustrate the upstream formation of a strong internal bore or gravity current. This upstream response is not of the undular type seen previously, but one that maintains the distinguishing features of a turbulent internal hydraulic jump. The observations also show the subsequent disintegration of this internal hydraulic jump into a packet of solitary internal waves that propagate into the far field, upstream of the sill. The internal hydraulic jump forms before relaxation of

Corresponding author address: Patrick Cummins, Institute of Ocean Sciences, 9860 W. Saanich Rd., Sidney, BC V8L 4B2, Canada.
E-mail: cumminsp@dfo-mpo.gc.ca

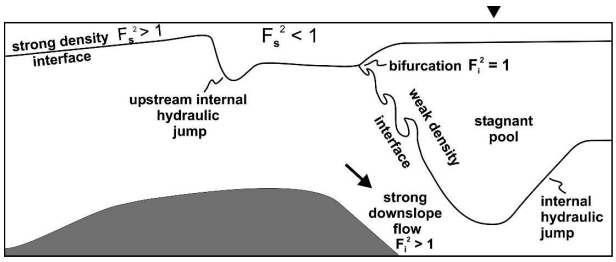

FIG. 1. Schematic diagram identifying the upstream internal hydraulic jump, along with salient features of a hydraulic sill flow.

the tidal flow and it is present simultaneously with the downslope hydraulic sill flow.

Figure 1 shows schematically the upstream hydraulic jump that is the focus of this study. Results presented below demonstrate that the character of the upstream response depends on a Froude number F_s based on the strong near-surface stratification and the flow speed of the upper layer. Figure 1 also includes the prominent features of a fully developed hydraulic sill flow. During the evolution to this state, the strong density interface near the surface undergoes a bifurcation, forming a new interface with a weak density step and a three-layer density structure. Entrainment of fluid across this unstable interface leads to the expansion of an overlying pool of stagnant, weakly stratified fluid (Farmer and Armi 1999a). As a consequence, a strong downslope flow develops over the lee side of the sill. The response in the vicinity of the crest is governed by a distinct interfacial Froude number F_i that is defined in terms of the weak density step and the lower-layer flow. A large hydraulic jump connects the supercritical downslope flow ($F_i > 1$) to conditions found farther downstream. With moderate tidal forcing, the bifurcation is located upstream of the sill crest, critical conditions ($F_i = 1$) prevail at the crest, and the flow is said to be in the crest-controlled regime. With sufficiently strong barotropic tidal forcing, the bifurcation is displaced downstream of the crest, as depicted in Fig. 1. (Such a transition is also shown in Fig. 4.) This is the "uncontrolled" flow state (Armi and Farmer 2002), and in this regime critical conditions occur at the bifurcation.

To help to interpret the observations presented in section 2, a two-dimensional nonhydrostatic model is applied to simulate the sill flow and the development of the upstream jump. Results from numerical experiments are presented in section 3 to examine the character of the upstream response as the strength of the near-surface stratification is varied. The simulations also show the development of solitary-like internal waves that propagate away from the sill as the tidal flow relaxes, consistent with the observations.

2. Observations

The observations were obtained from the region near the sill in Knight Inlet, British Columbia, Canada, the site of several previous studies of the interaction of stratified flow with topography (e.g., Farmer and Smith 1980; Farmer and Armi 1999a). Here we present new measurements made during spring tides in September 2002. The data were obtained from the Canadian Coast Guard Ship (CCGS) *Vector* equipped with a 200-kHz echosounder and a CTD. A small inflatable boat (hereinafter, the Zodiac) equipped with a 100-kHz echosounder and a 300-kHz ADCP was also used to collect data.

The focus is on an event observed during the ebb tide of 7–8 September 2002, which had a tidal range of approximately 4 m. The *Vector* first made an along-channel transect (transect 1) over the sill and then anchored just west of the sill crest (downstream on ebb tide), near the center of the inlet. The Zodiac was then deployed and data were acquired using instrumentation carried aboard both the *Vector* and the Zodiac. The location where the *Vector* was anchored and the path of the three transects are indicated in Fig. 2 on a bathymetric chart of Knight Inlet near Hoeya Head. The figure also includes an inset showing the time variation of the water level at nearby Glendale Cove, Knight Inlet, during the observational period.

An image of acoustic backscatter acquired with the *Vector*'s echosounder during transect 1 is shown in Fig. 3. This shows a plunging flow on the lee (west) side of the sill with large-amplitude instabilities on the interface of the downslope flow. The flow is in the crest-controlled regime in which the thickness of the lower-layer flow at the crest is about two-thirds of its upstream thickness. As is typically observed, a layer of stagnant fluid beginning at the bifurcation located at x= −150 m overlies the plunging downslope flow. The Kelvin–Helmholtz instabilities evident in Fig. 3 develop as a result of the large shear found along the interface between the stagnant layer and the plunging flow. The formation of the flow structure shown in Fig. 3 has been thoroughly documented by Farmer and Armi (1999a).

Following transect 1, the *Vector* was anchored close to the crest of the sill (see Fig. 2), while recording of acoustic backscatter data continued. At the anchor station the instrumented Zodiac was lashed alongside the ship near the stern and began recording acoustic backscatter and ADCP data. The *Vector*'s CTD was also deployed over the stern and began operation in a yo-yo cycling mode.

Time series of backscatter data from the *Vector* echosounder, Zodiac ADCP speeds, and the CTD data from

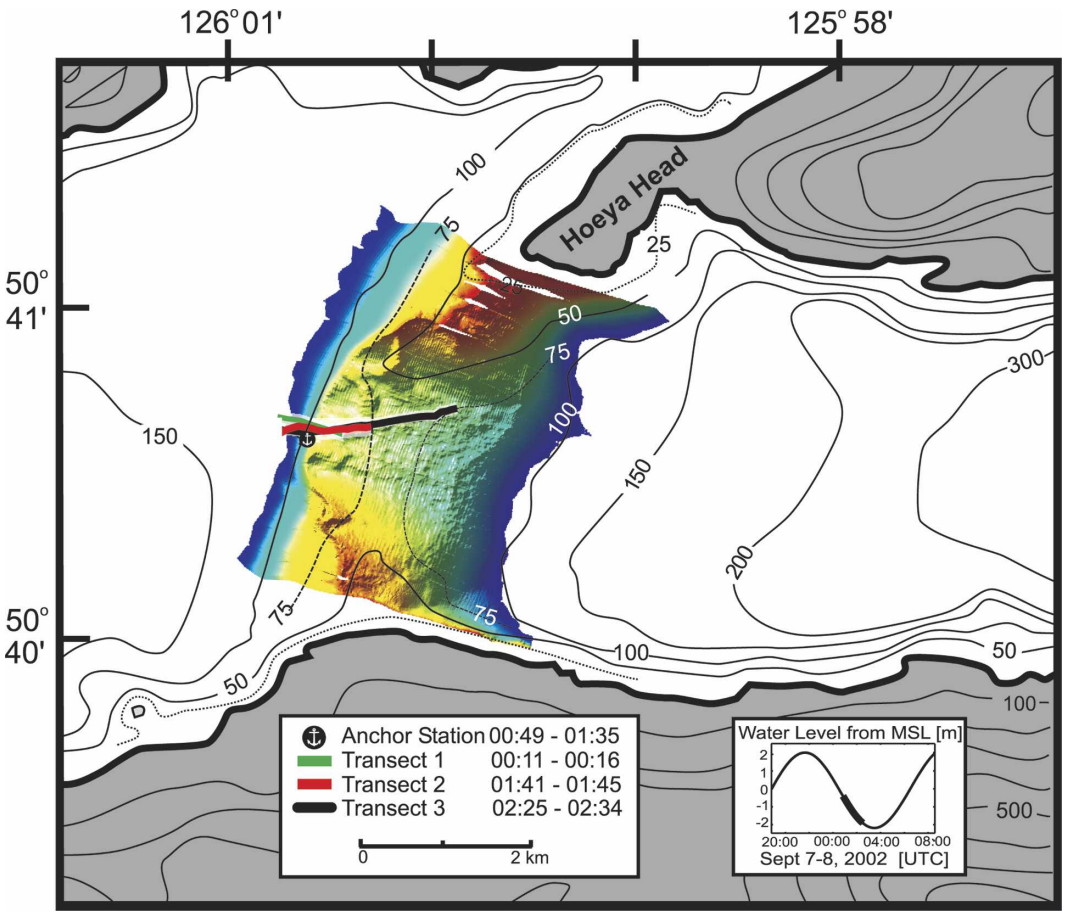

FIG. 2. Bathymetric map of Knight Inlet near Hoeya Head. The positions of the anchor station and the three transects are shown. The inset shows the tidal variation in water level at nearby Glendale Cove with the thickened portion of the curve corresponding to the observational period.

the anchor station are shown in Fig. 4. The salient feature is an initial rapid shoaling of the density and shear interface, the signature of which is evident in all of the instrumental records. The interface is shallowest in the echosounder data at 0053 UTC. This is followed by a more gradual deepening of the interface over the next half hour. Large-amplitude instabilities and overturning are evident near the beginning and especially at the end of the record.

The schematic diagrams along the top of Fig. 4 provide an interpretation of these data by relating the observations at the anchor station to changes in the large-scale structure of the flow. During time A, the flow is in the crest-controlled state observed in transect 1, as indicated in schematic A. Subsequently, the flow structure over the crest shifts downstream, accounting for the shoaling of the interface. Direct evidence for this motion is found by comparing the signal observed in the *Vector* echosounder, which is located amidship, with the record from the Zodiac ADCP, which was situated near the stern. The time of maximum shoaling is delayed in the ADCP record as the flow bifurcation first passes the echosounder and then the ADCP. A shorter time delay is also evident between the ADCP and the CTD records. All of this is consistent with the downstream displacement of the plunging flow structure, as shown in schematic B. This event is interpreted as a transition from the crest-controlled state A to the uncontrolled flow state B, which is described in detail by Armi and Farmer (2002). Such a transition arises because of an increase in the effective barotropic tidal forcing characterized by the Froude number associated with the barotropic forcing and the density step of the downslope flow. This occurs as mixing by instabilities on the plunging interface reduces the density difference between the downslope flow and that of the overlying stagnant pool. This leads to an increase in the relative strength of the barotropic forcing, which becomes sufficiently strong to drive the flow into the uncontrolled flow state.

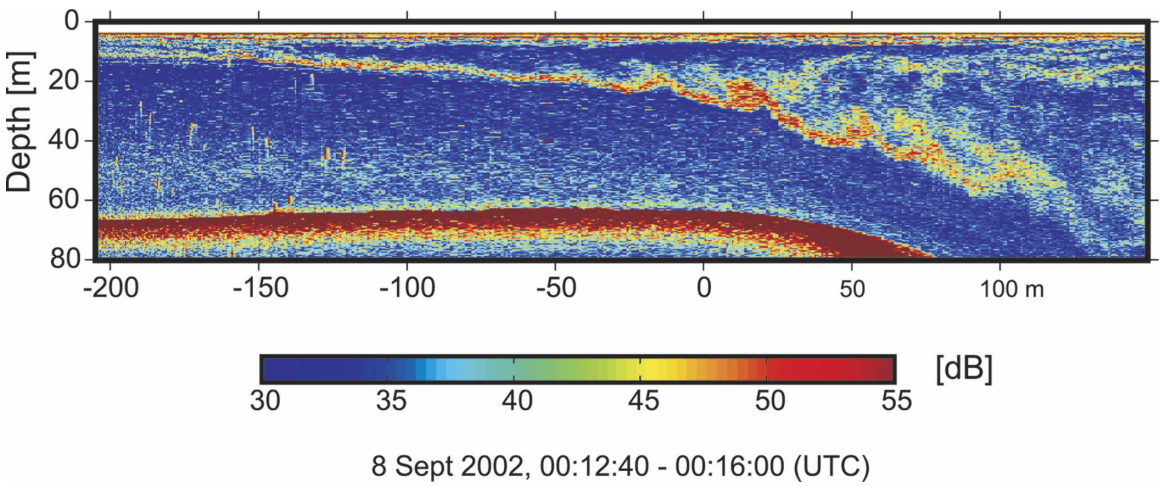

FIG. 3. Acoustic backscatter along transect 1 from the ship's echosounder. The data are presented at 1:1 aspect ratio with the upstream direction (east) on the left. The transect started 2 h 51 min following local high water.

Finally, with the gradual relaxation of the barotropic tide, the flow returns back to the crest-controlled state with a corresponding upstream shift in the flow structure. This is indicated in the schematic at time C in Fig. 4 and it is associated with the renewed observation of large-amplitude Kelvin–Helmholtz billows on the shear interface at the location of the anchor station.

At this time the surface expression of an internal hydraulic jump was observed and photographed from the bridge of the *Vector*. The Zodiac was then cast off from the ship to collect acoustic data. The top panel in Fig. 5 shows a photograph of the Zodiac heading up the inlet while collecting data along transect 2. Visible on the water surface just ahead of the Zodiac is a single pronounced surface slick, nearly spanning the width of the inlet, that is due to variations in sky reflection associated with modulation of small-scale surface ripples by the internal jump. It is worth noting that this feature was not observed to propagate upstream past the ship. Rather the slick developed about 350 m ahead of the ship and remained essentially stationary before advancing farther upstream.

The middle and lower panels in Fig. 5 present acoustic data along transect 2 (indicated in Fig. 2). A feature resembling a borelike intrusion is prominent in the echosounder and ADCP data. It is associated with strong shear and instabilities at a depth of 15–20 m. The nose of the bore is located 340 m upstream of the sill crest and coincides with the location of the photographed surface slick. Fluid in the surface layer is moving downstream relatively slowly (0.2–0.3 m s^{-1}), while in the lower layer it moves at a speed of nearly 1 m s^{-1}. The depth-averaged barotropic tidal flow along transect 2 was relatively strong (about 0.8 m s^{-1}). Thus, the ebb tidal flow had not yet relaxed and the plunging downslope flow is still present, although only a portion of it is evident in Fig. 5.

The rolled-under cleft found at the nose of the borelike intrusion in Fig. 5 appears to have the shape of an atmospheric dust front moving along the ground (Simpson 1997), inverted here in the oceanographic setting. The structure of the fluid velocity near the surface accounts for the presence of this feature. Figure 6 shows individual and averaged profiles of flow speed upstream and downstream of the nose of the jump at a vertical resolution of 2 m. Downstream of the bore (Fig. 6b) there is shear with an increase in speed indicated for the depth bin found closest to the surface. This is a robust feature appearing in all of the individual ADCP profiles. Since the upstream profiles (Fig. 6a) show almost no structure close to the surface, the shear is unlikely to be due to a surface wind stress. It may be associated with a very thin surface layer of freshwater; however, the data are insufficient to make this determination.

The echosounder data from transect 2 (Fig. 5) indicate the presence of small-scale turbulence along the shear interface. This is consistent with the laboratory experiments of Rottman and Simpson (1989). They showed that the character of internal bores depends on the amplitude parameter, $R = h_d/h_u$, where h_u and h_d are the thicknesses of the active surface layer upstream and downstream of the jump, respectively. The former is difficult to determine as there are no CTD measurements upstream of the jump. The acoustic backscatter suggests that $h_u \leq 3.5$ m and $h_d = 15$–18 m, so that $R \geq 4$. The possibility of vanishing h_u cannot be excluded, in which case the bore in Fig. 5 can be regarded as a

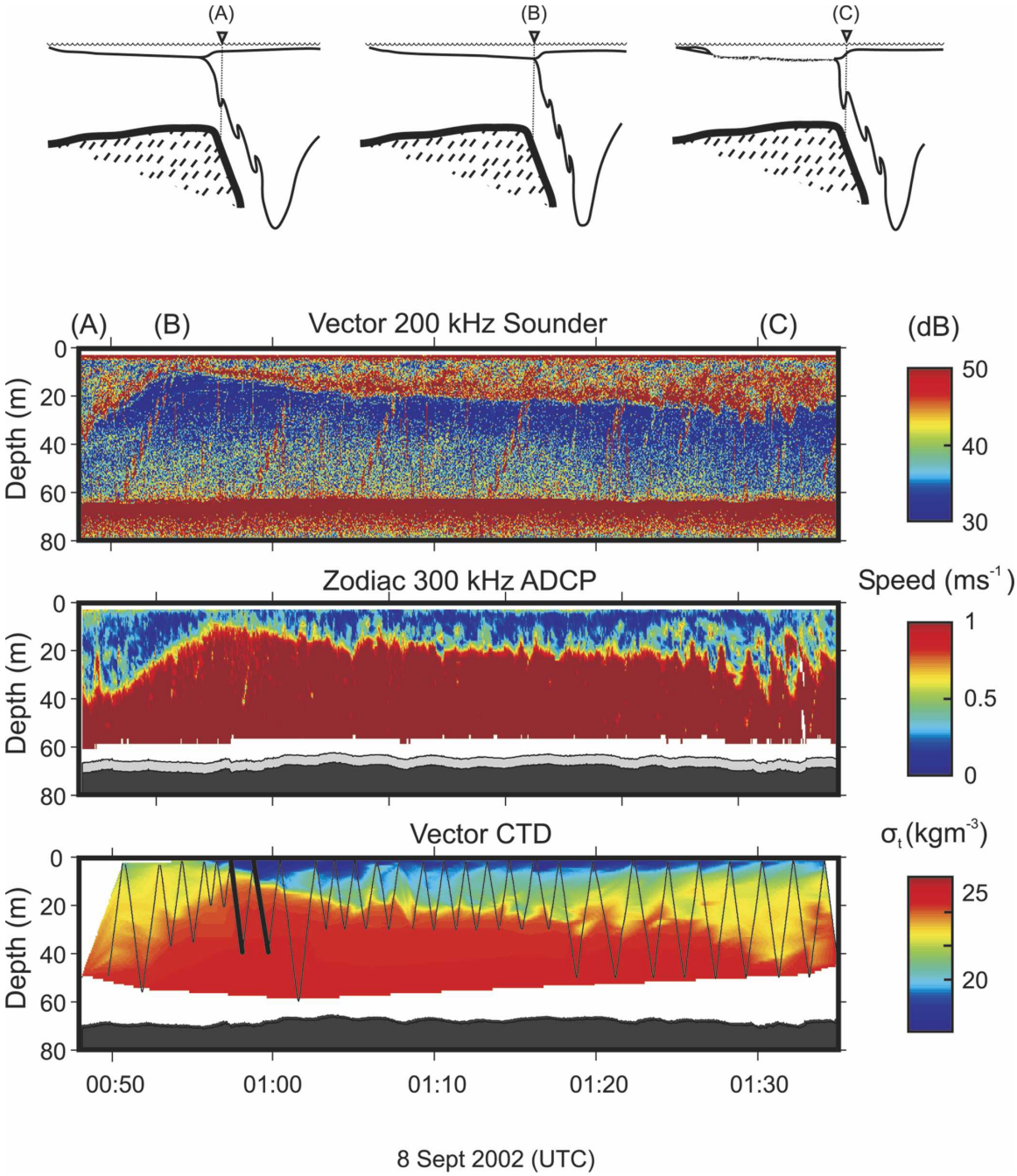

FIG. 4. Time series data with schematic diagrams at the top to provide an interpretation relating the observations at the anchor station to lateral displacements in the large-scale structure of the flow. Shown are (top) acoustic backscatter, (middle) ADCP flow speeds, and (bottom) σ_t, the fluid density, with the zigzag lines indicating the casts taken by the ship's CTD. The anchor station data start 3 h 28 min after local high water.

gravity current. As illustrated in Fig. 3 of Rottman and Simpson (1989), turbulent bores resembling gravity currents develop for $R > 3.5$–4. Smaller values of R are associated with internal bores of undular type, as have been observed previously in Knight Inlet (e.g., Farmer and Armi 1999b; Cummins et al. 2003).

Transect 3 (Fig. 7) was recorded about 40 min after transect 2. During the time between these two transects, the bore dispersed into a series of five solitary-like internal waves. The mean barotropic tidal flow along transect 3 is approximately 0.54 m s^{-1}. As the tidal flow weakened, the leading wave advanced up-

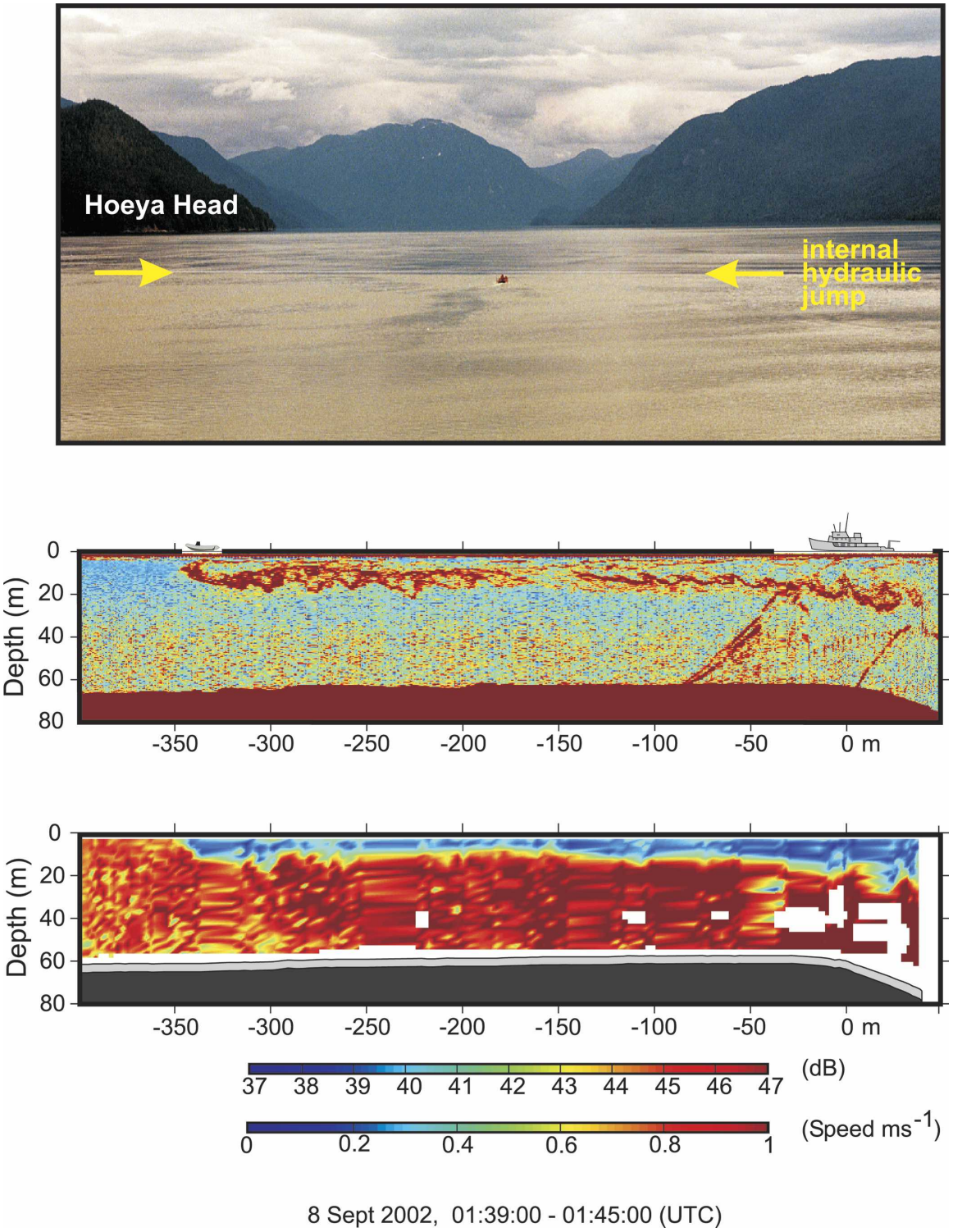

FIG. 5. (top) Photograph taken from the bridge of the CCGS *Vector* showing the Zodiac as it is approaching the nose of the hydraulic jump, along transect 2. (middle) Acoustic backscatter and (bottom) ADCP flow speeds are shown at a 1:1 aspect ratio. Approximate positions of the ship and the Zodiac at the time of the photograph are indicated above the middle panel. The ship's anchor chain is visible in the backscatter image. Transect 2 started 4 h 18 min after local high water.

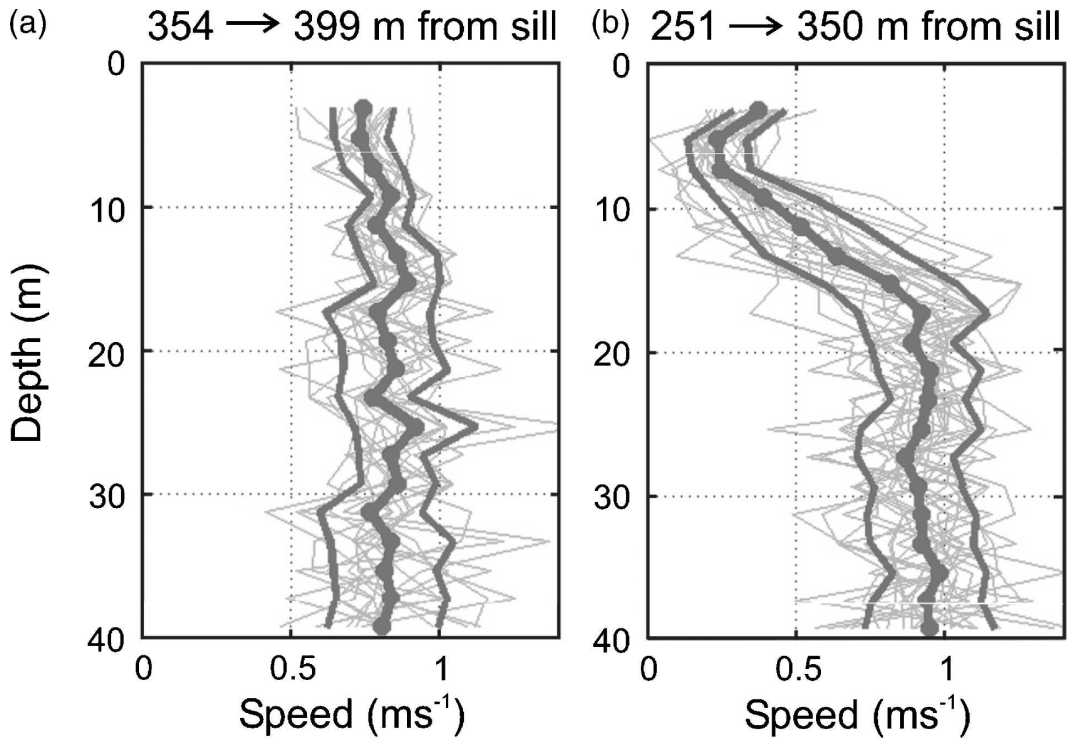

FIG. 6. Thin lines give individual vertical profiles of flow speed (a) upstream and (b) downstream of the nose of the internal hydraulic jump along transect 2. The thick lines indicate average profiles and standard deviations about the mean. The flow at all depths is in the downstream (west) direction.

stream and was located about 470 m ahead of the position of the nose of the bore in transect 2. The observations of Fig. 7 extend downstream of the sill crest and show the continued presence of the downslope hydraulic flow. This indicates that the flow remained controlled at the crest during the development of the nonlinear wave train. Thus, in contrast to the traditional view, the formation of the solitary waves preceded the relaxation and advance of the downstream depression.

The positions of the upstream disturbances in transects 2 and 3, together with the observed fluid velocities, invite an estimation of the speed of advance relative to the flow, which may be compared with theoretical models. A distance of 470 m separates the upstream limit of the jump and the wave train in the two transects, while the travel time is 40 min. Thus, the speed of the feature relative to the bottom is about 0.2 m s^{-1}. The depth-averaged flow speed during this interval had a mean value of about 0.65 m s^{-1}. Assuming that the convective speed is equal to that of the depth-averaged flow implies a propagation speed of 0.85 m s^{-1} relative to the flow.

Jump relations for the speed of advance of a bore in a two-layer system were developed by Wood and Simpson (1984) and Klemp et al. (1997). The former assumes that energy is conserved in the contracting layer, while the latter model is based on energy conservation in the expanding layer. With dissipation in both layers, the bore speed lies between these limiting values (Li and Cummins 1998). For a large bore advancing into a thin layer, it is appropriate to apply the relation of Klemp et al. (1997):

$$\frac{u_K}{\sqrt{g'h_d}} = \left[\frac{R(rR-1)(rR+r-2)}{rR^2-3rR+R+1}\right]^{(1/2)}, \qquad (1a)$$

where $r = h_u/H$. Here, H is the total fluid depth and g' is the reduced gravity. In the limit of vanishing upstream layer thickness ($h_u \to 0$), (1a) reduces to the gravity current relation of Benjamin (1968):

$$\frac{u_B}{\sqrt{g'h_d}} = \left[\frac{(1-\alpha)(2-\alpha)}{1+\alpha}\right]^{(1/2)}, \qquad (1b)$$

with $\alpha = h_d/H$. Density profiles taken from the *Vector* CTD casts (Fig. 8) suggest a value of $g' = 0.05$–0.06 m s^{-2}. With $(h_u, h_d) = (3\text{ m}, 15\text{ m})$ and an overall depth $H = 65$ m, (1a) yields an intrinsic bore speed, $u_K = 0.88$–0.96 m s^{-1}, similar to the gravity current speed of $u_B = 0.91$–1.00 m s^{-1} obtained from (1b). These values are slightly larger than the estimate of 0.85 m s^{-1} based

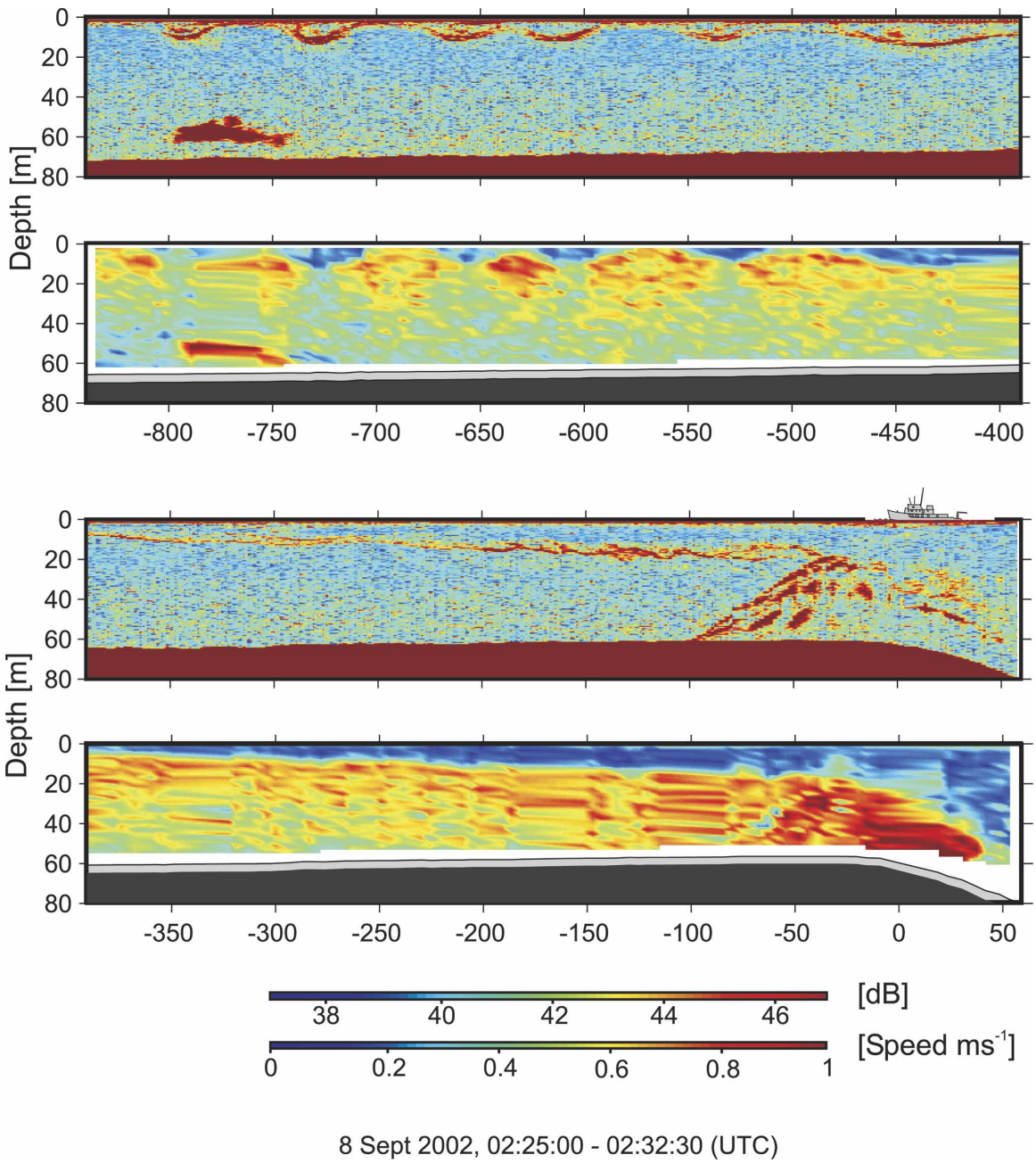

FIG. 7. Acoustic backscatter and ADCP flow speeds along transect 3. The transect is shown in two sections to present the data at 1:1 aspect ratio. For each section the top panel shows the acoustic backscatter and the bottom panel shows the flow speeds. The high backscatter found just above the bottom at 60-m depth between −800 and −750 m is likely due to a school of fish. The transect started 5 h 4 min after local high water.

on the observations. Given the approximations involved in applying two-layer models to a continuously stratified fluid, these calculations suggest that propagation characteristics of the features identified in transects 2 and 3 are consistent with theoretical expectations for a large-amplitude internal bore or a gravity current.

3. Numerical simulations

The results of numerical simulations with a two-dimensional, nonhydrostatic model are now considered. Rather than attempting to replicate the observations in exact detail, the intent here is to identify the processes and parameters governing the upstream re-

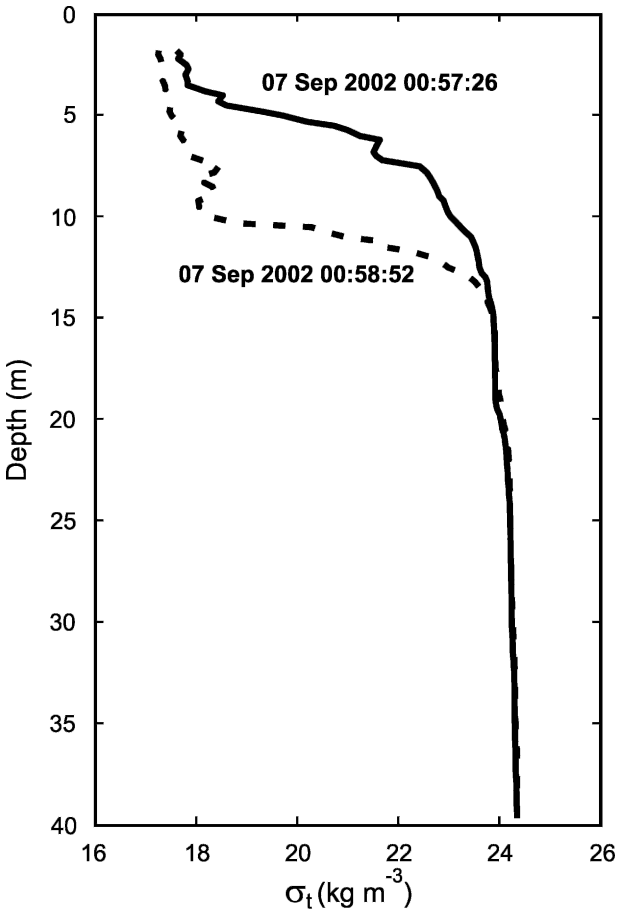

FIG. 8. Vertical density (σ_t) profiles from two CTD casts at the anchor station. The two casts are indicated by the thick lines in the bottom panel of Fig. 4.

sponse in the context of a tidally varying flow. The model is similar to that described by Cummins et al. (2003) and is based on a vorticity–streamfunction formulation of the equations of motion. Coupled equations for the advection of vorticity and density are solved using the flux-correct transport method of Zalesak (1979). There is no explicit diffusion of density or vorticity, except near the bottom boundary. Here, the vertical mixing coefficients are given a simple Gaussian dependence with an *e*-folding vertical scale of 5 m. The bottom boundary condition for vorticity is specified according to the no-slip condition. This is necessary to assure separation of the bottom boundary layer, which typically is observed on the lee side of the sill in Knight Inlet during the early stages of ebb tide. [See Farmer and Armi (2001) for a discussion of this matter.] The model domain is an inflow–outflow channel with a horizontal extent of 10 240 m and a maximum depth of 200 m. Variable bottom topography representing the sill is specified over the inner 4500 m of this domain. The grid has a uniform horizontal resolution of 5 m and a vertical resolution of 1 m.

Results are presented from three numerical experiments in which the model is started from rest with a laterally homogeneous density field. Vertical density profiles for the three cases are illustrated in Fig. 9. While the stratification below 10 m has an identical small variation with depth, a pronounced density gradient of varying strength is specified near the surface. The most strongly stratified experiment has essentially the same density profile as used in Cummins et al. (2003). There is a second case with a moderate near-surface stratification, and a third experiment with a relatively weak stratification. The linear density variation specified for the surface layer is a practical idealization of the time-dependent stratification observed in the vicinity of the sill (e.g., Fig. 8). It is less prone to spurious numerical dispersion than a steplike density structure and provides a reasonable representation of the near-surface stratification.

For each experiment the model is integrated over a

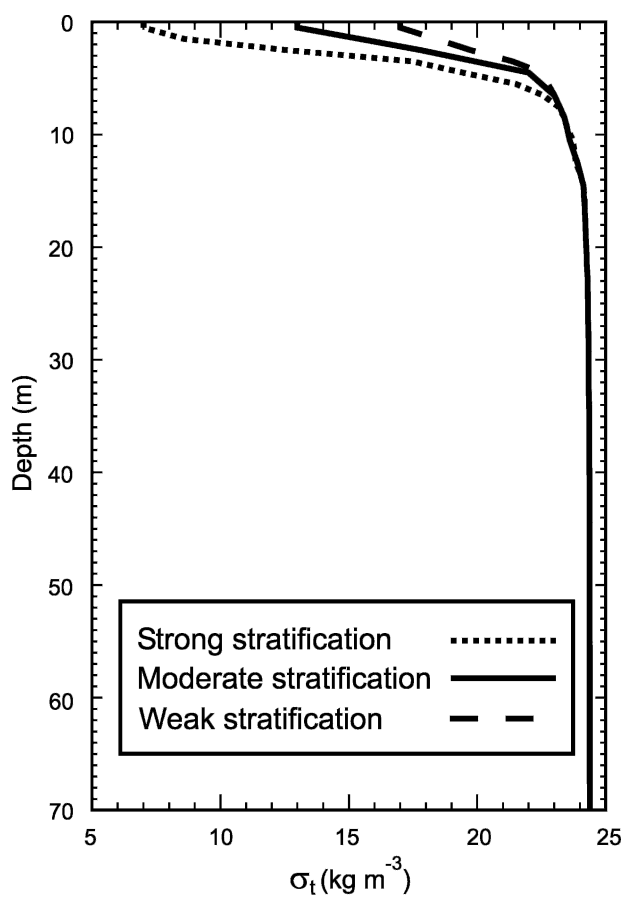

FIG. 9. Vertical profiles of the initial density field for the three basic numerical experiments with weak, moderate, and strong stratification near the surface.

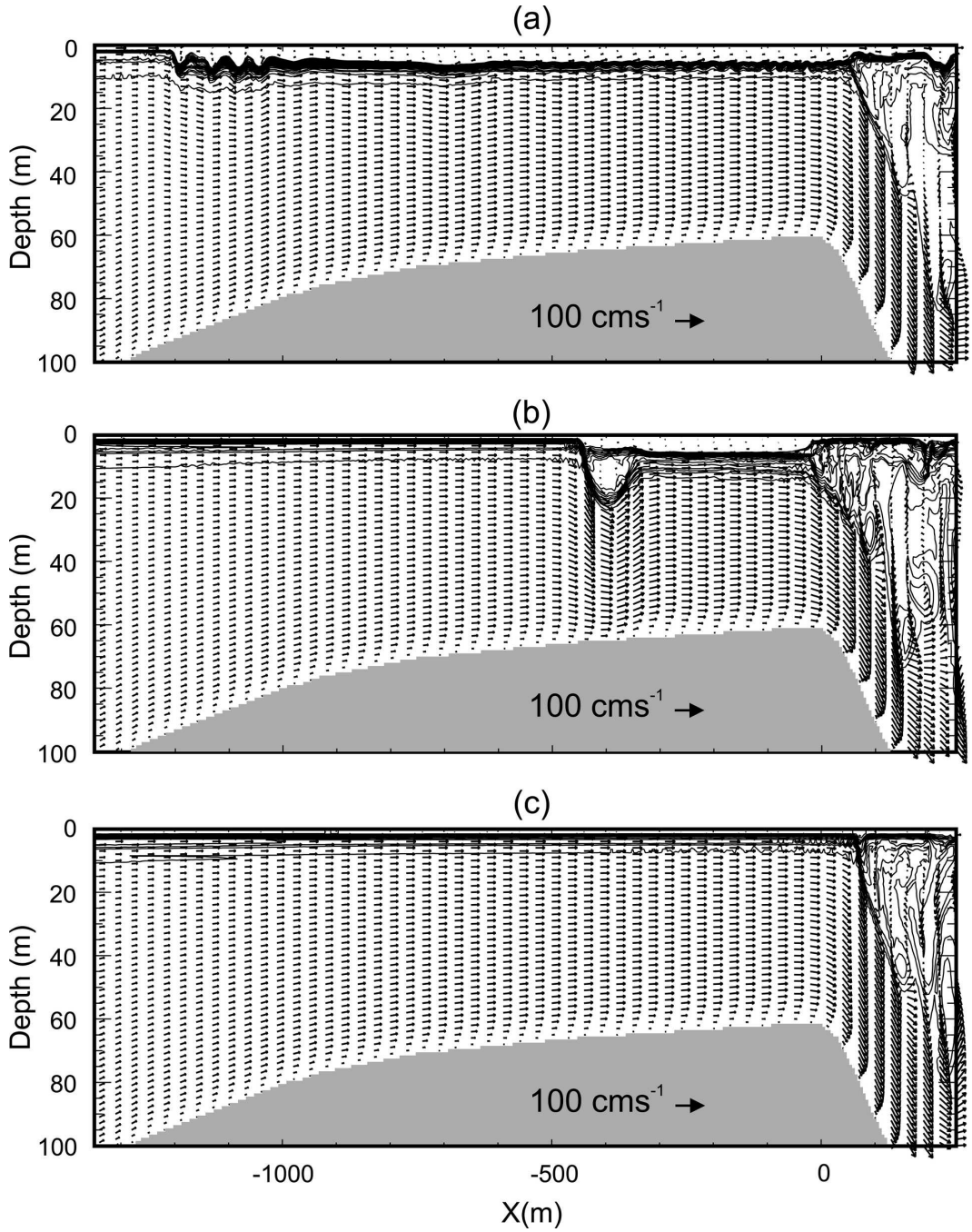

FIG. 10. Density contours and flow vectors from the numerical experiments with (a) strong, (b) moderate, and (c) weak near-surface stratification at 4 h and 10 min. The instantaneous barotropic flow rate is 41.2 $m^2\ s^{-1}$. Density contours are drawn at intervals of 0.5 kg m^{-3} over σ_t = 17–23 kg m^{-3}. Additional contours are drawn for σ_t = (23.75, 24, 24.25). Flow vectors are shown for every sixth grid point in the horizontal and every second grid point in the vertical. Note that only the inner portion of the computational domain is illustrated here.

half tidal period with the barotropic transport per unit width given by $Q(t) = Q_o \sin[(2\pi t)/T]$, where T = 12.42 h and Q_o = 48 $m^2\ s^{-1}$. This leads to a peak barotropic speed over the sill crest of 0.8 m s^{-1}, consistent with the value predicted from (2) of Farmer and Smith (1980) for a semidiurnal tide with a range of 4 m (see inset in Fig. 2).

Figure 10 illustrates the structure of the fully devel-

oped flow over the sill for the three experiments after 4 h 10 min have elapsed following the start of the tidal forcing. In each case an unstable downslope flow develops over the lee side of the sill. An internal hydraulic jump matches this supercritical flow with conditions found farther downstream (cf. Fig. 1). Overlying the downslope flow is a pool of stagnant, weakly stratified fluid that is separated from the downslope flow by a relatively weak density step ranging in magnitude from 0.5 kg m^{-3} close to the crest to about 0.2 kg m^{-3} downstream of the crest. Since this is characteristic of the three experiments, the interfacial Froude numbers associated with the downslope flow are comparable in each case.

As in the observations in Fig. 4 and those discussed by Armi and Farmer (2002), the flows in these experiments are strongly forced in the sense that the flow bifurcation is displaced downstream of the sill crest at some point in each simulation. In Figs. 10a and 10c the bifurcation at 4 h 10 min is still downstream of the crest, whereas for the intermediate case of Fig. 10b it has already retreated upstream slightly with the relaxation of the barotropic tide. In the other two cases, the bifurcation subsequently retreats back upstream of the sill crest with further relaxation of the barotropic tide.

The most prominent feature of the upstream region in Fig. 10b is an internal hydraulic jump located about 450 m upstream of the sill crest, in general agreement with the observations discussed in section 2. In contrast, Fig. 10c shows no such jump, while a weaker undular jump appears considerably farther upstream in Fig. 10a. In the intermediate case of Fig. 10b the nose of the bore conforms approximately with the classical 60° angle of intersection with the surface (von Kármán 1940), in contrast to the rolled-under cleft of the observed jump in Fig. 5.

The time-dependent response of the three numerical experiments upstream of the sill crest is now considered. Figures 11a–f show the position of a single isopycnal from each experiment at successive times through the simulations. In each case the reference isopycnal has an initial undisturbed depth of 4.5 m. The initial response is illustrated in Fig. 11a, which shows the isopycnals 1 h 15 min following the start of the simulations. A sloping interface is evident with isopycnals shoaling upward in the upstream direction. This is associated with a first-mode subcritical response to the slowly modulated barotropic tidal forcing. This response is the result of rapidly propagating long waves emitted along upstream characteristics (Stoker 1957; Baines 1995, section 2.3). In a slowly evolving flow, the lowering of interfacial depth reflects the variation in pressure of the Bernoulli function required to compensate for the increase in kinetic energy due to spatial acceleration of the flow over the shoaling bottom.

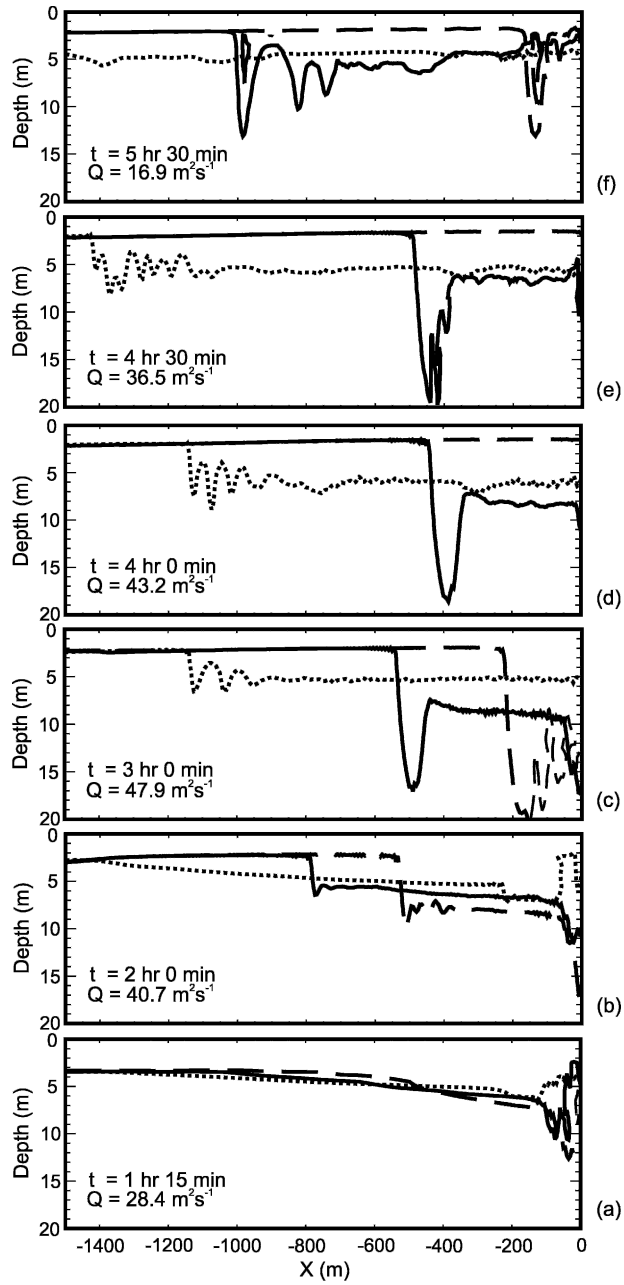

FIG. 11. Position of isopycnals through different stages of ebb tide. The σ_t = (22.5, 22, 19.43) kg m^{-3} isopycnals for the weakly, moderately, and strongly stratified experiments are drawn with dashed, solid, and dotted lines, respectively. The initial undisturbed depth of each isopycnal is 4.5 m. The panels are arranged with time increasing upward.

Figure 11b (2 h) shows the presence of an internal hydraulic jump at $x = -800$ m for the case with moderate stratification. Downstream of the jump, the isopycnal slopes gently downward toward the crest, while a

weak upward slope has developed upstream. The weakly stratified case has developed a similar jump of larger amplitude at $x = -550$ m. On the other hand, a jump has yet to develop in the strongly stratified experiment, and the interface still retains its subcritical downward slope. However, the interface in this case is starting to steepen at about $x = -1350$ m, indicating the incipient formation of a jump. The early stages of interfacial steepening are also evident in Fig. 11a for the weakly stratified case at about $x = -500$ m.

At 3 h (Fig. 11c), the internal hydraulic jumps of the intermediate and weakly stratified cases have increased in amplitude and been displaced downstream from their position at 2 h, as a result of the increasing tidal flow. In addition, a weaker undular bore is now evident in the strongly stratified experiment, similar to the case studied in Cummins et al. (2003). Note that in each experiment the interface upstream of the jumps has acquired a weak upward slope.

Figure 11d shows the upstream response at 4 h. By this time, the bore in the weakly stratified experiment has been displaced downstream of the crest, where it is lost. In contrast, the bores in the moderate and strongly stratified experiments are almost stationary. In the latter case, numerous undulations develop at the front, whereas the intermediate case retains the character of a strong internal hydraulic jump.

The last two panels from this series (Figs. 11e and 11f) show the response with slackening of the tidal flow. The undular bore in the strongly stratified case quickly escapes upstream. In the moderately stratified simulation, the bore is practically stationary over the period $t = 3$–5 h. It is released upstream about 5 h following the start of the tidal flow and disperses into a group of rank-ordered solitary waves. This is comparable to the observations of section 2, where the release of solitary waves occurs between 4 h 30 min and 5 h following local high water. In the weakly stratified experiment, the upstream region remains featureless until near the very end of the ebb tidal flow. At this point, large-amplitude solitary waves are emitted upstream, one of which is visible at $x = -150$ m in Fig. 11f. In all cases the isopycnal that had shoaled upward in the far field is restored to approximately its initial depth by the passage of the upstream-propagating disturbances.

It is useful to consider the numerical simulations in terms of a Froude number for the surface layer. As shown in appendix A, for a thin, linearly stratified surface layer of thickness $2h_r$ overlying a deep unstratified lower layer, the Froude number is given by

$$F_s = \frac{\pi u_s}{4\sqrt{g' h_r}}, \tag{2}$$

where u_s is the average flow speed of the surface layer and $g' = g(\rho_r - \rho_s)/\rho_r$ is the reduced gravity. Here, ρ_s is the value of the density at the surface ($z = 0$) and ρ_r is the density of a reference isopycnal whose local depth, denoted h_r, is at middepth within the stratified surface layer. Equation (2) is used to provide an estimate of the Froude number associated with the near-surface layer of the model. As indicated above in Fig. 1, F_s is distinguished from the interfacial Froude number based on the weak density step separating the downslope flow from the overlying stagnant pool.

The reference isopycnal used to calculate F_s has an initial upstream depth of 4 m, approximately middepth in the highly stratified surface layer (Fig. 9). In addition, F_s is not very sensitive to small variations in the choice of ρ_r.

Contour plots of $F_s(x, t)$ are presented in Fig. 12 for the upstream region of the three numerical experiments. An initial subcritical response ($F_s < 1$) is evident in Fig. 12. Eventually, in each case, critical conditions ($F_s = 1$) develop at some point over the sill, well upstream of the crest. This occurs earlier and closer to the crest in the weakly stratified case and later and farther upstream in the strongly stratified experiment. Shortly afterward, an upstream bore develops, appearing initially at the location along the $F_s = 1$ contours indicated by the arrows in Fig. 12. The local contours of F_s subsequently converge, forming a sharp gradient that indicates the position of the bore. In each case, the flow is supercritical ($F_s > 1$) on the upstream side of the bore, and subcritical on the downstream side.

Supercritical conditions gradually extend upstream over the sill. Near the midpoint of the simulations, as the barotropic tidal forcing reaches its maximum, the supercritical region extends over the entire region between the bore and a point near the leading edge of the topography. (The upstream limit of the topography is indicated by vertical dotted lines in Fig. 12.) In the weakly stratified experiment, as the bore is swept downstream, supercritical conditions prevail over the entire topography upstream of the sill crest. With the relaxation of the barotropic tidal flow, F_s decreases and the supercritical region contracts as the bore is released. Figure 12 shows that subcritical conditions are reestablished in the wake of the advancing bores in the strongly and moderately stratified cases.

It is worth noting that maximum Froude numbers attained over the sill exceed considerably values that may be estimated from the initial stratification and the peak barotropic tidal flow. For example, with the moderate stratification and a maximum tidal speed of 0.6 m s^{-1} [$Q(t) = 48$ m^2 s^{-1} and a depth of 80 m at $x = -1000$ m], the Froude number is $F_s = 0.86$. In contrast to this

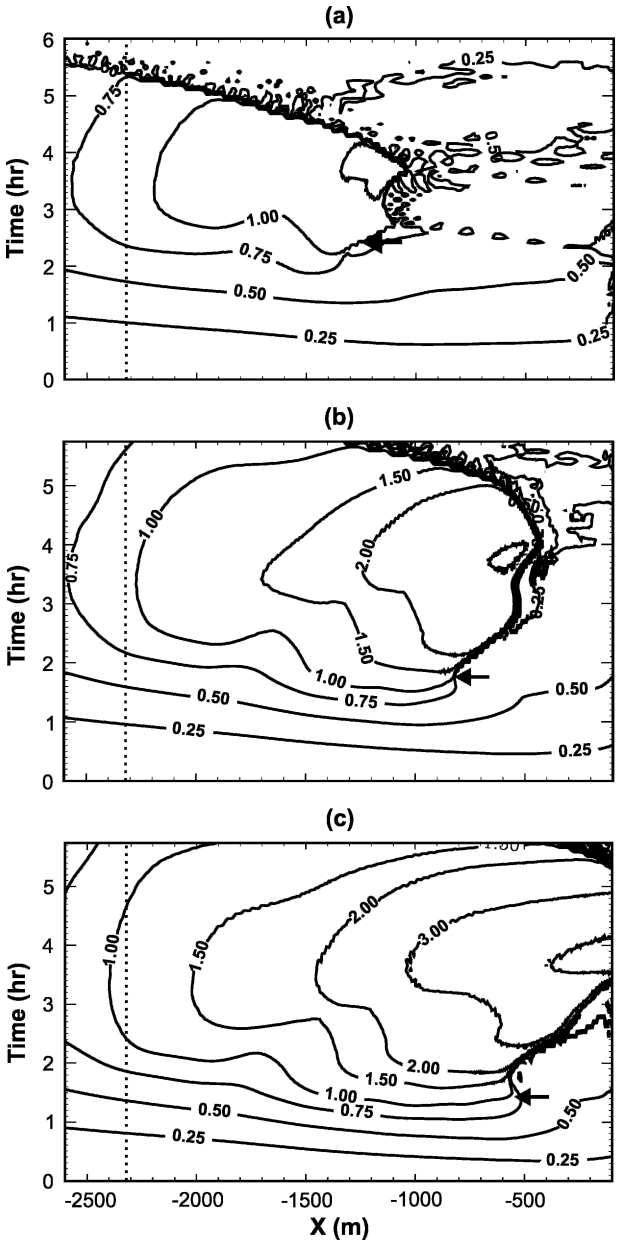

FIG. 12. Contour plots of $F_s(x, t)$ from the (a) strongly, (b) moderately, and (c) weakly stratified numerical experiments. The tip of the arrow in each frame shows the (x, t) position where an upstream jump is first identified in the simulations. The vertical dotted lines indicate the upstream edge of the sill topography of the model.

subcritical value, Fig. 12b shows that values of $F_s > 2$ are reached over this region. The reason for this difference is discussed in the next section.

4. Discussion

To elucidate the response of the model and, by implication, the observations, it is useful to apply the theory of two-layer hydraulic flows. For quasi-steady, hydrostatic flow over a two-dimensional sill, the slope of the density interface is given by (10c) of Armi (1986), which, in the absence of a lateral contraction, reduces to

$$\frac{dh_1}{dx} = \frac{-F_2^2}{1 - G^2}\frac{dH}{dx}. \tag{3}$$

Here, the composite Froude number G is defined by $G^2 = F_1^2 + F_2^2$, where $F_1 = u_1/\sqrt{g'h_1}$ and $F_2 = u_2/\sqrt{g'h_2}$ are Froude numbers for the upper and lower layers, respectively. The flow speed and thickness of the upper (lower) layer are given by u_1 (u_2) and h_1 (h_2), respectively. Here, $H = (h_1 + h_2)$ is the total fluid depth, and g' denotes the interfacial reduced gravity. Note that the Froude number F_s given by (2) is analogous to F_1, but for a linearly stratified upper layer.

In response to the initially weak tidal flow, the simulations show that a slope in the near-surface density interface develops over the upstream region in accordance with (3). Provided the flow is subcritical ($G^2 \approx F_1^2 < 1$), the shoaling bottom ($dH/dx < 0$) requires that the interface slopes downward ($dh_1/dx > 0$) in the flow direction. This interfacial slope is evident in all three cases shown in Fig. 11a and consistent with the subcritical flow conditions indicated in Fig. 12.

The initial subcritical adjustment of the near-surface interface occurs via long waves that propagate rapidly upstream, producing a finite-amplitude shoaling of the interface in the far field (Baines 1995, sections 2.2 and 3.6). Figure 11 clearly shows the resulting upward displacement of the isopycnals from their initial undisturbed depth of 4.5 m. The characteristic speed of long internal waves propagating in the upstream (negative x) direction is given by

$$\lambda = u_{\mathrm{con}} - \left\{\frac{h_1 h_2}{H^2}[g'H - (u_1 - u_2)^2]\right\}^{1/2}, \tag{4}$$

where $u_{\mathrm{con}} = (u_1 h_2 + u_2 h_1)/H$ is the convection speed (Armi 1986). The uplifting of the near-surface interface increases the convective speed of the flow and reduces the intrinsic wave speed. As a result, the leading edge of these long waves advances more rapidly into the far field than the trailing edge. These are then rarefaction waves that spread out with time. Figure 1 of Lawrence (1993) includes a schematic depicting the uplifting of a density interface by an upstream-propagating rarefaction.

Closer to the crest, the subcritical response lowers the interface because of the spatial acceleration of the flow over the shoaling bottom (e.g., Figs. 11a and 11b). As conditions vary in response to the intensifying tidal forcing, these adjustments are communicated continu-

ously upstream along wave characteristics. Because of the dependence of the wave speed on upper-layer thickness in (4), the characteristics eventually intersect forming a discontinuity and leading to local steepening of the interface (see Fig. 2.6a of Baines 1995).

With the increasing tidal flow, the Froude number of the surface layer increases and eventually supercritical conditions develop immediately upstream of the discontinuity or jump (Fig. 12). It is the uplifting of the interface through the initial subcritical adjustment that permits strongly supercritical conditions to develop as the tidal forcing increases. Over the supercritical region ($G^2 \approx F_1^2 > 1$), the two-layer hydrostatic theory (3) predicts that the interface will slope upward ($dh_1/dx < 0$) in response to the decreasing fluid depth. This upward slope is evident upstream of the jumps in Figs. 11b–d, in accordance with (3). (The schematic diagram in Fig. 1 included an exaggerated upward tilt to the upstream interface.)

Closer to the sill crest, but still upstream, the interface is deeper and the Froude number remains smaller than unity. Thus, there must be a transition between the supercritical and subcritical regions (e.g., Fig. 12b) and this requires the presence of an internal hydraulic jump. In the vicinity of such a transition the assumptions of energy conservation and hydrostatic pressure that form the basis for the hydraulic theory break down, leading to energy losses and to the nonhydrostatic overshoot at the leading edge of the jump.

In the weakly stratified experiment, as the upstream Froude number becomes very large, the jump is displaced downstream of the crest. This leaves supercritical conditions (Fig. 12c) with a shoaling interface ($dh_1/dx < 0$) over the entire upstream region of the topography up to the bifurcation point (e.g., Fig. 10c). The resulting flow state is suggestive of the steady-state approach controlled flow (Lawrence 1993). However, the time dependence of the barotropic forcing is a significant factor complicating identification of this flow regime. This matter is taken up in appendix B.

5. Conclusions

This study has combined field observations and numerical simulations of stratified flow over a sill to examine the generation of upstream internal hydraulic jumps and solitary waves. The observations of 7–8 September 2002 from Knight Inlet show the development of a turbulent internal bore or gravity current upstream of the sill crest under conditions of strong ebb flow. These observations complement previous measurements of weaker undular bores at this location (Farmer and Armi 1999b; Cummins et al. 2003) and demonstrate that a range of upstream responses is possible. Toward the end of ebb tide, the jump disperses into an upstream-propagating group of large-amplitude solitary waves. In contrast to the well-known model of Maxworthy (1979), the development of these nonlinear waves occurs independently of and prior to the relaxation of the large pycnocline depression found on the lee side of the sill.

To simulate the generation of upstream disturbances in a tidally modulated flow, a set of numerical experiments was conducted in which the strength of the stratification near the surface was varied. Two additional experiments in which the maximum flow rate is varied are described in appendix C. The numerical results show that the generation of an upstream jump depends on a Froude number, F_s, based on the flow rate and stratification of the fluid layer near the surface. As the tidal flow intensifies, supercritical conditions ($F_s > 1$) develop over the sill, upstream of the crest. Thus, the development of an upstream internal hydraulic jump is required to match the upstream region with the subcritical conditions that prevail closer to the crest.

As the maximum value of F_s attained during the tidal flow varies, the response ranges from a weak undular bore found well upstream of the sill crest for small F_s, to a strong, nearly stationary jump much closer to the crest for intermediate values of F_s. If the Froude number becomes sufficiently large during the tidal cycle, the upstream jump may be swept downstream of the crest, where it is lost. The intermediate case is the one in which the modeled jump mostly closely resembles the observed one. The principal discrepancy concerns the shape of the leading edge, which in the observations has a rolled-under appearance associated with shear close to the surface. Near the end of the model simulation, as the tidal flow is waning, a packet of upstream-propagating internal solitary waves is formed in accordance with the observations.

Acknowledgments. We are grateful to David Farmer for discussions and assistance with the field program. We thank Peter Chandler and Lizette Beauchemin for help in the preparation of the figures and manuscript. Mark Trevorrow kindly provided the high-resolution bathymetry of the Knight Inlet sill illustrated in Fig. 2. Useful comments received from two anonymous referees are gratefully acknowledged.

APPENDIX A

Froude Number for a Thin, Linearly Stratified Upper Layer

A Froude number for a fluid with a thin, linearly stratified upper layer, $F_s = u_s/c$, is defined similarly to

the upper-layer Froude number of two-layer hydraulic theory. Accordingly, the convective speed u_s is taken as the flow speed averaged over the upper layer and c is the first-mode long-wave speed. The latter is determined from the equation governing the vertical normal modes,

$$\frac{d^2w}{dz^2} + \frac{N^2}{c^2} w = 0, \tag{A1}$$

subject to boundary conditions $w(0) = w(-H) = 0$, where $z = -H$ is the bottom and $z = 0$ is the surface. The vertical stratification is assumed to consist of a thin upper layer of constant buoyancy frequency N_o and thickness $2h_r$ overlying a deep unstratified layer. Thus,

$$\begin{aligned} N &= N_o, \quad -2h_r \le z \le 0, \\ N &= 0, \quad -H \le z < -2h_r, \end{aligned} \tag{A2}$$

where $N_o = \sqrt{g'/h_r}$ and $g' = g\,(\rho_r - \rho_s)/\rho_r$. Here, the fluid densities are given by $\rho_r = \rho(-h_r)$ and $\rho_s = \rho(0)$.

For the stratified upper layer, the solution to (A1) may be written as $w = A\,\sin(z/z_o)$, while for the lower layer, $w = B(z + H)$, where A and B are both constants. Substituting into (A1) we obtain

$$c = N_o z_o, \tag{A3}$$

where z_o is a constant that is determined by requiring that w and dw/dz are continuous at $z = -2h_r$. This yields a transcendental equation

$$\tan\gamma + \left(\frac{H}{2h_r} - 1\right)\gamma = 0, \tag{A4}$$

with $\gamma = 2h_r/z_o$.

In analogy with the reduced-gravity hydraulics of a single-layer fluid, we consider the limit of an infinitely deep lower layer such that (A4) reduces to $\tan\gamma = -\infty$ and $z_o = 4\,h_r/\pi$ for the first internal mode. The Froude number is then $F_s = (\pi u_s/4\sqrt{g'\,h_r})$.

This expression for the Froude number is approximate because the influence of shear on the phase speed c has been neglected. In the two-layer model (4), this assumption is valid provided that $[1 - (u_1 - u_2)^2/g'H]^{1/2} \simeq 1$, a condition that is generally well satisfied over the upstream region in the numerical experiments. In the reduced-gravity limit, $H \simeq h_2 \to \infty$, the convective speed $u_{\rm con} \to u_1$, and (4) reduces to $\lambda = u_1 - (g'h_1)^{1/2}$. The shear between the two layers has no influence on the phase speed in this limit.

APPENDIX B

Steady-State Integrations

The upstream bore in Fig. 10b (also illustrated schematically in Fig. 1), is "quasi steady" in the sense that it is almost stationary over a significant portion of the tidal cycle. It is of interest to determine whether the upstream bore in Fig. 10b is maintained under steady forcing. Accordingly, additional experiments were conducted with the barotropic forcing given by

$$\begin{aligned} Q(t) &= Q_o \sin\left(\frac{2\pi}{T}t\right), \quad 0 \le t \le \frac{T}{4} \\ Q(t) &= Q_o, \qquad\qquad \frac{T}{4} < t \le \frac{T}{2}, \end{aligned} \tag{B1}$$

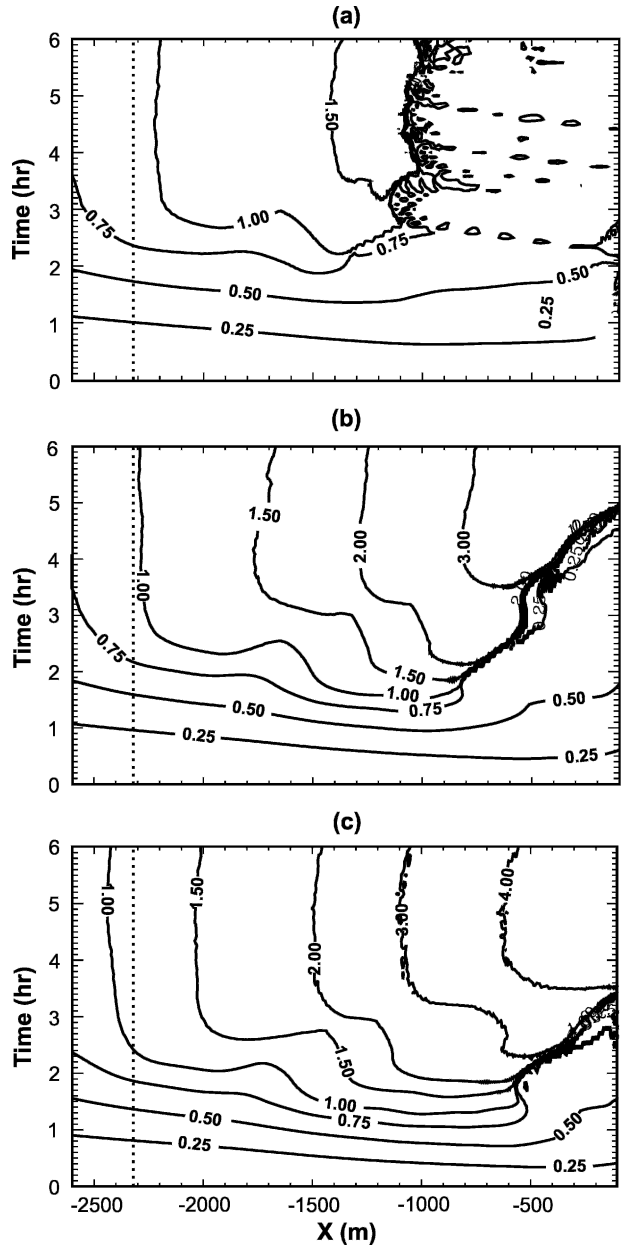

FIG. B1. Contour plots of $F_s(x, t)$ from the steady-state experiments of appendix B with (a) strong, (b) moderate, and (c) weak near-surface stratification. The vertical dotted lines indicate the upstream edge of the sill topography of the model.

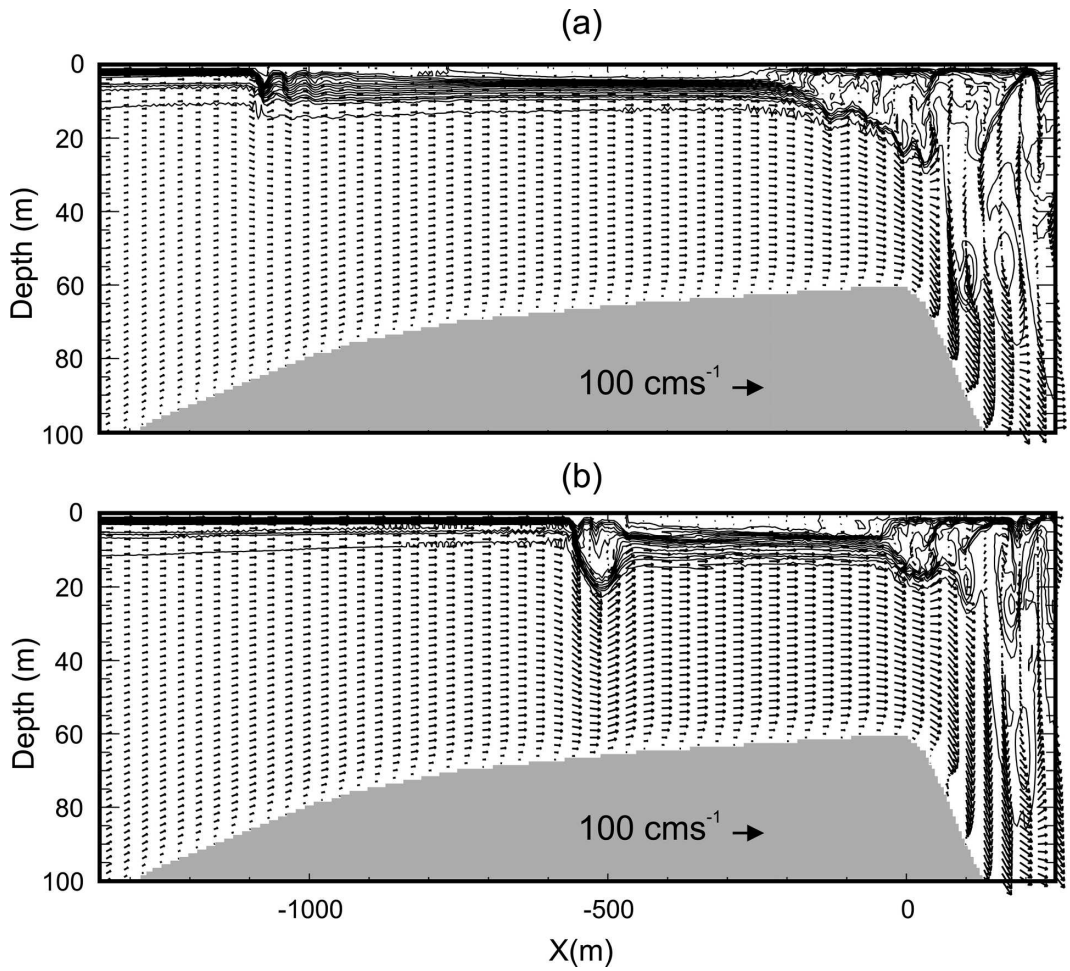

FIG. C1. Density contours and flow vectors at 3 h 40 min from two additional experiments discussed in appendix C with the weak stratification and reduced flow rates. The instantaneous flow rate is (a) 28.8 and (b) 36.5 $m^2\ s^{-1}$. Contour levels for σ_t are as in Fig. 10.

where, as above, T = 12.42 h and Q_o = 48 $m^2\ s^{-1}$. Results with varying near-surface stratification are presented in terms of contour plots of $F_s(x, t)$ in Fig. B1. The lower half of each plot is identical to the tidally forced cases shown in Fig. 12. With constant barotropic forcing in the second half of the integrations, the flows upstream of the sill crest tend toward steady state. In the case with moderate near-surface stratification, Fig. B1b shows that the upstream bore is eventually swept downstream. Evidently, it is the waning barotropic tidal flow that permits the bore to maintain its position upstream of the crest in the tidally modulated simulation (Figs. 11 and 12b). In the steady state, the $F_s = 1$ contour in Fig. B1b is aligned rather closely with the leading edge of the topography, and there is a supercritical flow over the entire upstream portion of the sill. This is indeed the approach-controlled flow regime discussed in detail by Lawrence (1993); thus, the upstream bore can be regarded as a transient in the transition to this flow regime.

The case with weak stratification (Fig. B1c) also appears to tend toward the approach-controlled regime. In this case, the $F_s = 1$ contour extends a short distance upstream of the leading edge of the topography. This is probably due to frictional effects that determine the exact position of the control (Lawrence 1993). On the other hand, in the case with strong stratification (Fig. B1a) the upstream jump remains trapped over the sill to the end of the simulation. This suggests the possibility of a hybrid steady-state flow with a jump connecting an approach-controlled regime to a subcritical flow closer to the crest. Further work is required to establish whether this is a true steady-state flow configuration. However, it is clear from all of these simulations that

the time scale for the establishment of the approach-controlled flow regime over the Knight Inlet sill is not small in comparison with the M_2 tidal period.

APPENDIX C

Froude Number Scaling

The numerical results in section 3 suggest a scaling for the upstream response based on the Froude number of the surface stratification. To examine this idea further, two additional experiments were conducted in which the model was initialized with the weak stratification shown in Fig. 9. In these cases the peak volume flux, Q'_o, was adjusted such that

$$Q'_o = Q_o \sqrt{\frac{\Delta\rho'}{\Delta\rho}}, \tag{C1}$$

where, as above, $Q_o = 48\ \mathrm{m^2\ s^{-1}}$. In (C1) $\Delta\rho' = 6.3$ kg m^{-3} represents the density difference across the 8-m-thick surface layer with the weak stratification and $\Delta\rho$ represents the density change across the surface layer of either the moderate (10.3 kg m^{-3}) or strong (16.3 kg m^{-3}) stratification. The scaling implied by (C1) indicates that with $Q'_o = 38\ \mathrm{m^2\ s^{-1}}$ the upstream response will consist of a strong, internal hydraulic jump, similar to the case with moderate stratification presented above. Likewise with $Q'_o = 30\ \mathrm{m^2\ s^{-1}}$, a weaker undular jump is anticipated, as in the strongly stratified case of section 3.

Figure C1 shows flow fields and density contours from the two additional experiments at 3 h 40 min following the start of the tidal forcing. The expected responses are confirmed: with the weak stratification and $Q'_o = 38\ \mathrm{m^2\ s^{-1}}$, the response consists of a strong, quasi-stationary jump located about 500 m upstream of the sill crest, until it is released near the end of the simulation. With $Q'_o = 30\ \mathrm{m^2\ s^{-1}}$, a weaker undular jump is formed much farther upstream. The positions of the jumps are similar to the respective cases discussed above at comparable times.

While the flow in Fig. C1a has a similar upstream response to the case shown in Fig. 10a, there is a different response in the vicinity of the sill crest. Because of the weaker barotropic forcing, the flow bifurcation is found upstream of the crest in Fig. C1a and the flow is in the crest-controlled regime. In contrast to the case shown in Fig. 10a, the strongly forced regime is never attained during this simulation. Thus, while the upstream hydraulic response depends on the upstream Froude number of the surface layer, it appears to be independent of whether the sill flow enters into the strongly forced flow regime. This finding is contrary to the suggestion of Cummins et al. (2003) that a rapid transition to the uncontrolled state of the strongly forced regime is important to the upstream response.

REFERENCES

Armi, L., 1986: The hydraulics of two flowing layers with different densities. *J. Fluid Mech.,* **163,** 27–58.

——, and D. M. Farmer, 2002: Stratified flow over topography: Bifurcation fronts and transition to the uncontrolled state. *Proc. Roy. Soc. London,* **458A,** 513–538.

Baines, P. G., 1995: *Topographic Effects in Stratified Flows*. Cambridge University Press, 482 pp.

Benjamin, T. B., 1968: Gravity currents and related phenomena. *J. Fluid Mech.,* **31,** 209–243.

Cummins, P. F., S. Vagle, L. Armi, and D. M. Farmer, 2003: Stratified flow over topography: Upstream influence and generation of nonlinear internal waves. *Proc. Roy. Soc. London,* **459A,** 1467–1487.

Farmer, D. M., and J. D. Smith, 1980: Tidal interaction of stratified flow over the sill in Knight Inlet. *Deep-Sea Res.,* **27A,** 239–254.

——, and L. Armi, 1999a: Stratified flow over topography: The role of small scale entrainment and mixing in flow establishment. *Proc. Roy. Soc. London,* **455A,** 3221–3258.

——, and L. Armi, 1999b: The generation and trapping of solitary waves over topography. *Science,* **283,** 188–190.

——, and ——, 2001: Stratified flow over topography: Models versus observations. *Proc. Roy. Soc. London,* **457A,** 2827–2830.

Holloway, P. E., E. Pelinovsky, T. Talipova, and B. Barnes, 1997: A nonlinear model of internal tide transformation on the Australian North West Shelf. *J. Phys. Oceanogr.,* **27,** 871–896.

Jackson, C. R., 2004: *An Atlas of Internal Solitary–like Waves and Their Properties*. 2d ed. Global Ocean Associates, 560 pp. [Available from Global Ocean Associates, 6220 Jean Louise Way, Alexandria, VA 22310; or online at http://www.internalwaveatlas.com/Atlas2_index.html.]

Klemp, J. B., R. Rotunno, and W. C. Skamarock, 1997: On the propagation of internal bores. *J. Fluid Mech.,* **331,** 81–106.

Lawrence, G. A., 1993: The hydraulics of steady two-layer flow over a fixed obstacle. *J. Fluid Mech.,* **254,** 605–633.

Li, M., and P. F. Cummins, 1998: A note on hydraulic theory of internal bores. *Dyn. Atmos. Oceans,* **28,** 1–7.

Maxworthy, T., 1979: A note on the internal solitary waves produced by tidal flow over a three-dimensional ridge. *J. Geophys. Res.,* **84,** 338–346.

Rottman, J. W., and J. E. Simpson, 1989: The formation of internal bores in the atmosphere: A laboratory model. *Quart. J. Roy. Meteor. Soc.,* **115,** 941–963.

Simpson, J. E., 1997: *Gravity Currents in the Environment and the Laboratory.* 2d ed. Cambridge University Press, 244 pp.

Stoker, J. J., 1957: *Water Waves.* Interscience, 567 pp.

von Kármán, T., 1940: The engineer grapples with non–linear problems. *Bull. Amer. Math. Soc.,* **46,** 615–683.

Wood, I. R., and J. E. Simpson, 1984: Jumps in layered miscible fluids. *J. Fluid Mech.,* **140,** 215–231.

Zalesak, S. T., 1979: Fully multidimensional flux-corrected transport algorithms for fluids. *J. Comput. Phys.,* **31,** 335–362.